Earth and Planetary Science Letters 579 (2022) 117365

Contents lists available at ScienceDirect

Earth and Planetary Science Letters

www.elsevier.com/locate/epsl

Fault roughness controls sliding instability

Doron Morad [a,b], Amir Sagy [b], Yuval Tal [a], Yossef H. Hatzor [a,*]

[a] Dept. of Earth and Environmental Sciences, Ben-Gurion University of the Negev, Beer-Sheva 84105, Israel
[b] Geological Survey of Israel, Yesha'yahu Leibowitz 32, Jerusalem 9692100, Israel

ARTICLE INFO

Article history:
Received 10 August 2021
Received in revised form 22 November 2021
Accepted 3 January 2022
Available online xxxx
Editor: R. Bendick

Keywords:
friction
roughness
dilation
slip dynamics
stick-slip
earthquakes

ABSTRACT

The frictional strength of faults controls the stability and the dynamics of slip in diverse natural phenomena including earthquakes, induced seismicity, and landslides. It has been shown that geological faults and rock discontinuities in general are rough in a wide range of scales but the dependency of slip dynamics on surface roughness for a large spectrum of heights has never been measured. Here we show specifically how slip dynamics dramatically varies as a function of surface roughness using direct shear experiments performed on laboratory-generated faults in Diabase. We demonstrate experimentally that under relatively low normal stress of 5 MPa, stick-slip oscillations, commonly referred to as laboratory earthquakes, only occur in a very limited range of roughness values within which a specific level, defined here as the *critical roughness*, triggers the highest amplitude of oscillations. Sliding across roughness higher or lower than critical is typically stable. Using monitored vertical motions through slip (dilation) coupled with numerical modelling we show that sliding on extremely "smooth" surfaces is typically stable because the very small height of asperities does not allow for the nucleation and motion arrest required for 'stick' phases to ensue, whereas sliding on extremely rough "fractured" surfaces is typically characterized by shearing through the tall asperities. Sliding across "sawcut" surfaces, however, is found to be particularly susceptible to stick slip deformation, and the shear motion is shown to be purely dilatant where the dilation and compression of the sliding interface are in phase with the stick slip oscillations. We conclude therefore that dilatant shear across moderately rough interfaces is a prerequisite for stick slip oscillations and consequently, for sliding instability.

1. Introduction

Slip surfaces are natural occurrences of shear existing in a wide range of scales, from micro-flaws in minerals, through macro scale of rock joints, and up to mega-scale faults along tectonic plate boundaries. Because frictional strength between surfaces is determined by the area of discrete contact zones and by their strength (Bowden and Tabor, 1950; Dieterich and Kilgore, 1994; Rubinstein et al., 2004), the topography of the surfaces is one of the major parameters affecting their frictional behaviour (Archard, 1957; Mei and Wu, 2021; Persson et al., 2005). The topography of rock surfaces varies from extremely smooth and polished (Siman-Tov et al., 2013) to rough and undulating (Candela et al., 2012; Power et al., 1987) depending on their dimensions, material properties and deformation history (Power et al., 1988; Sagy and Brodsky, 2009). Roughness of rock discontinuities has been recognized very early on as a dominant factor controlling the maximum shear resistance under relatively low normal stresses (Patton, 1966) while later experimental observations further demonstrated that slip dynamics and its transition from stable to unstable slip vary for different initial surface roughness (Goebel et al., 2017; Ohnaka, 1973; Okubo and Dieterich, 1984). Although Byerlee (1978), in his pioneering experimental work on rock friction, concluded that the maximum friction of faults at seismogenic depths is not affected by roughness, later experimental studies suggest that indeed fault irregularities and surface roughness are critical for slip nucleation and dynamics also at high seismogenic stresses as they strongly influence and modify the contact characteristics (Aubry et al., 2020; Goebel et al., 2017; Harbord et al., 2017).

Shallow earthquakes, events of induced seismicity, glacier sliding, and landslides runout may also be susceptible to instabilities associated with sliding across rough interfaces. Moreover, dilatant shear across rough interfaces can modify the critical pore pressure level required to induce slip (Brantut, 2020).

Experiments and theory suggest that the condition for slip to be unstable is governed by the relationship between the stiffness of the rock body surrounding the faults (k) and a critical stiffness of the interface (k_c), which is governed by the fault frictional

* Corresponding author.
E-mail address: hatzor@bgu.ac.il (Y.H. Hatzor).

https://doi.org/10.1016/j.epsl.2022.117365
0012-821X/

properties and normal stress (Rice and Ruina, 1983; Ruina, 1983). Slip will be unstable when $k_c > k$, and because the stiffnesses are physical properties of both structure and material, surface geometry and its evolution are expected to affect k (Dieterich and Smith, 2009; Fang and Dunham, 2013) and k_c (Tal et al., 2020) values, and accordingly the slip dynamics, even under high tectonic stresses (Aubry et al., 2020; Harbord et al., 2017). A particularly interesting case is of stick-slip oscillations which are associated with cycles of quasi-static phases followed by spontaneous slip events. These frictional oscillations have been referred to as "laboratory earthquakes" because they are believed to represent an analogue model of natural faulting (Brace and Byerlee, 1966; Scuderi et al., 2016).

While discontinuity surfaces in rocks are rough in a wide range of scales (Power et al., 1987), the dependency of slip dynamics on surface roughness has rarely been measured, in particular for a large spectrum of heights. Here we show by a series of direct shear experiments on Diabase interfaces how friction, dilation, and slip dynamics dramatically vary as a function of initial surface roughness. We confirm numerically that surface geometry indeed governs slip dynamics and in particular, affects the magnitude of laboratory earthquakes during sliding instabilities. Because the focus of this study is on the influence of initial roughness on slip dynamics, we chose to perform all experiments on the same rock type (Diabase) and under the same normal stress level. We chose to perform our tests under an imposed constant normal stress of 5 MPa as this level of normal stress was found by us in previous studies to represent the transition from slip weakening to slip hardening in direct shear experiments of granite sawcut surfaces (Biran et al., 2009) and the transition from slip smoothening to slip roughening in direct shear experiments of fractured limestone surfaces (Badt et al., 2016). Further research under higher normal stresses will be necessary in order to extend the validity of our results to seimogenic depths. The results of this study are nevertheless immediately applicable to the analysis of sliding instabilities in diverse geological processes including catastrophic rock slides (e.g. Ibanez and Hatzor, 2018), landslides (e.g. Fan et al., 2017), and induced seismicity due to changes in surface reservoir levels (e.g. Gupta, 2002) or fluid injection into reservoirs underground (e.g. Fang et al., 2017).

2. Materials and methods

2.1. The starting material

The starting material for all tests is commercially available Diabase from Shanxi Black Granite Quarry in China. This Shanxi Diabase, so named by the quarry, is medium-grained (mean grain size of 0.4 mm) composed of 40% Plagioclase, 40% Clinopyroxene, 10% Amphibole and 10% oxides and other minerals. The bulk density and porosity are 3.05 $\frac{gr}{cm^3}$ and 0.73%, respectively. Static Young's modulus and Poisson's ratio of the intact rock material obtained under uniaxial compression using the TerraTek triaxial system at BGU rock mechanics laboratory (for technical details see (Shitrit et al., 2019)) are 97 GPa and 0.19 ± 0.02, respectively. Acoustic velocities of the intact material were tested in the Vinci Acoustic Velocity System at BGU rock mechanics laboratory (for technical details see (Gordin et al., 2020) and the obtained dynamic Young's modulus and Poisson's ratio are 119 GPa and 0.24, respectively.

2.2. Sample preparation and surface roughness analysis

Six levels of initial roughness are studied here, named Fracture A, B, C, Sawcut, and Polished A, B (see Fig. 1). The Fracture interfaces were created by four-point bending of solid Diabase prisms, thus obtaining pure tensile fractures. Fracture A (with sample-scale RMS = 1356 μm) is characterized by higher RMS compared to Fracture B (RMS = 450 μm), where the RMS is the root mean squares of the deviation of the surface from planarity (See detailed description below). Fracture-C is a polished version of Fracture B obtained using 180 # polishing grit and sandpaper (RMS = 410 μm). The intermediate roughness specimen is Sawcut, with RMS of 7 μm. Polished A interface was obtained by polishing a sawcut interface with 1000# polishing powder grit with characteristic RMS of 0.85 μm. Finally, the smoothest interface, Polished B was obtained by polishing a Sawcut interface using 1 μm diamond suspension, with characteristic RMS of 0.7 μm. The average interface size used for direct shear testing is 10 cm length by 9 cm width, with the lower interface length typically fixed at 12 cm to ensure proper contact between the upper and lower blocks throughout the shearing segments, to minimize end effects. The samples are then cast in steel templates that are positioned in the shear box.

The initial roughness profiles of Fracture A, B, C and Sawcut interfaces were measured at the Geological Survey of Israel using a 3D laser profilometer model type Conoscan-10 manufactured by Optimet. Typical resolution of the profilometer is 1-5 μm depending on the material and geometry of the scanned surface. The polished surfaces were scanned at the Racah Institute of Physics of the Hebrew University of Jerusalem using nano-scale resolution white light interferometer manufactured by OptiWorks. The measurements of Polished A post shear were taken perpendicular to shear direction in order to better identify roughness variability after sliding. Each scanned sample consisted of 10^5 to 10^6 measurement points.

To quantify surface roughness, we calculate the values of the root mean square (RMS) heights (average deviation of the topography from a planar surface) along parallel profiles in a given direction by:

$$RMS_x = \left[\frac{1}{L}\int_0^L Y^2(x)dx\right]^{0.5} \quad (1)$$

where L is the profile length, Y is the amplitude or height of a given point, and x is the distance along the profile in a given direction. Every calculated value is the average RMS of all the parallel profiles in a given length L along the surface. Maximum RMS values for Fractures A - C and for the Sawcut interfaces are calculated for profiles parallel to the slip direction with lengths of 9 cm along the surface. We note that the maximum length of the entire apparent contact area between the surfaces (~10 cm) is slightly larger. RMS values of the Polished-A and B samples are measured based on profile lengths of 6 cm that represent well the entire surface because the RMS values at larger scales vary only slightly due to the polishing process (see Fig. 1D).

3. Experimental setup

Direct shear experiments are performed using a hydraulic, closed-loop servo-controlled system at BGU rock mechanics laboratory (Fig. 2). Normal and shear load capacities are 1000 kN and 300 kN respectively, with load cells linearity of 0.5% Full Scale. Two horizontal and four vertical LVDTs monitor horizontal and vertical displacement of the interface, respectively, during shear. The LVDTs range is 50 mm with 0.25% linearity Full Scale. Data acquisition rate is set to 50 Hz (50 counts per sec.) in all displacement and load channels. Experiments are conducted at room temperature of 26 °C and relative humidity of ~41% in dry interface conditions.

The experiments are performed under an imposed constant normal stress of 5 MPa and load point (shear piston) velocity of $v_0 = 0.01$ mm/s. The experimental procedure begins with lowering the normal piston at a constant load rate of 0.01 MPa/s until

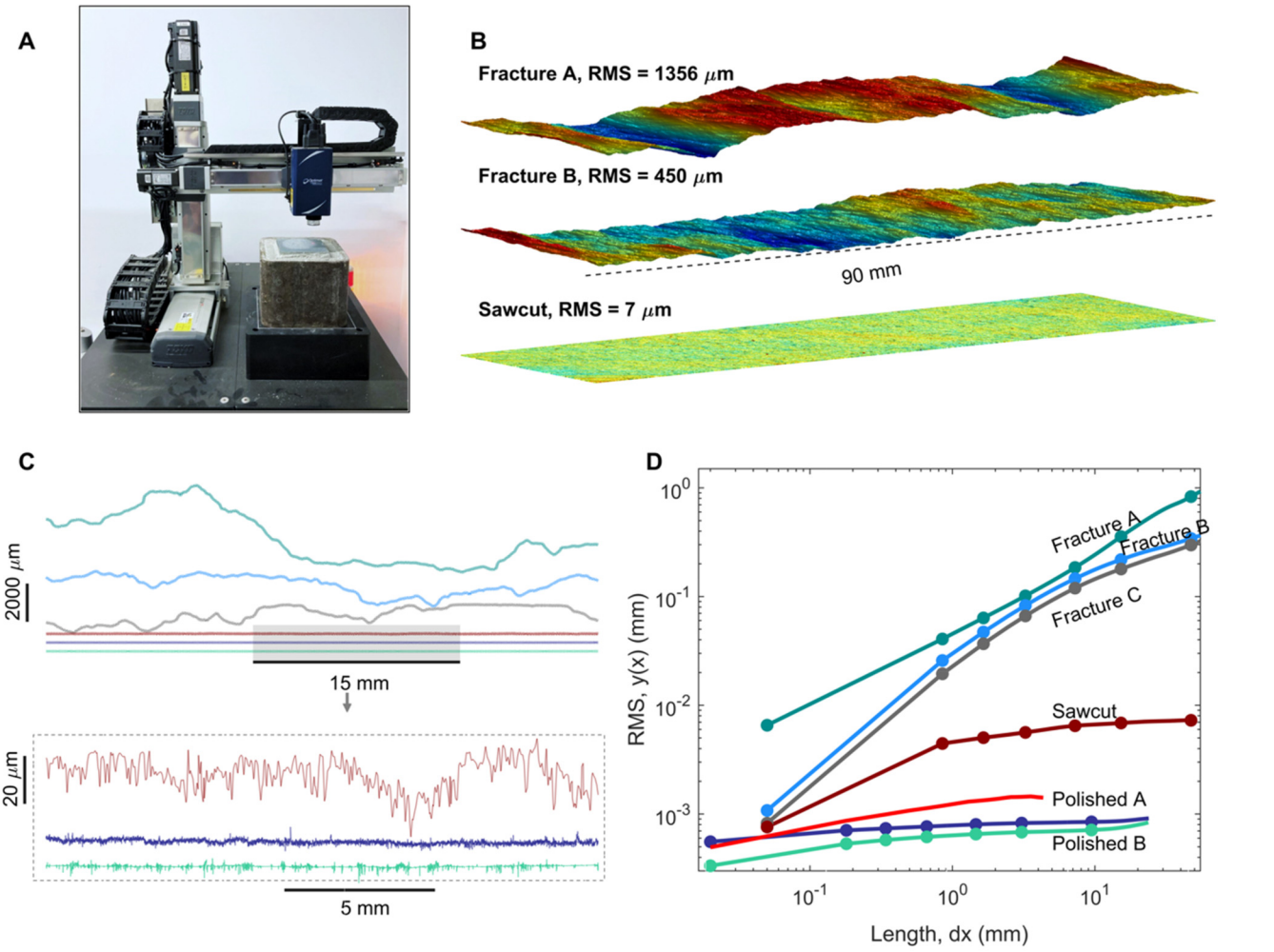

Fig. 1. Wide spectrum of roughness levels, with RMS values ranging from 1356 μm (Fracture A) to 0.7 μm (Polished B). A) The 3D Conoscan-10 laser profilometer used in this research, B) 3D illustration of "Fracture A", "Fracture B", and the "Sawcut" surfaces, C) 2D profiles of the six initial roughness levels with vertical exaggeration of X 12 (in bottom panel detailed plot of the "Sawcut", "polished A" and "Polished B" surfaces with vertical exaggeration of X 750), D) Initial RMS roughness for all tested surfaces as a function of sampling profile length in the shear direction.

the 5 MPa target normal stress is reached while the interface is held at a fixed position. A constant normal stress boundary condition is then imposed during the shear segments, so that the interface is free to dilate or contract during shear, the vertical displacement of which is monitored by the four vertical LVDTs that are attached to the shear box (Fig. 2A). The sliding target is typically set to 10–13 mm as monitored from the two horizontal LVDTs that are attached to the shear box very close the tested interface (Fig. 2B). The Fracture interfaces are initially set in a fully mating configuration, but after several millimetres of displacement the interfaces are not fully coupled of course. Because the constant displacement rate is imposed on the shear piston, the block is free to accelerate forward during stick-slip instabilities and its dynamic displacement is closely monitored by the two horizontal LVDTs. After a slip event, loading is resumed at the prescribed piston displacement rate while the response of the block continues to be monitored by the two horizontal LVDTs.

The characteristics of the stick-slip events in all experiments are studied in great detail. The "stick" velocity (v_{stick}), "slip" velocity (v_{slip}), and stress drop ($\Delta\tau$) in each stick-slip cycle are measured from the output of the two horizontal LVDTs and the load cell, respectively. The characteristics of the stick-slip cycles are typically measured after the interface has sheared at least 4 mm, well beyond the peak shear stress obtained in each tested interface. To distinguish between electric noise and real stick-slip events in the case of lower amplitude oscillations, a real stick slip is defined when the spontaneous change from maximum to minimum shear stress within a single stick-slip cycle is at least one order of magnitude higher than the resolution of the shear load cell.

4. Calculation of stiffnesses and velocities

4.1. Experimental determination of the machine stiffness k_m

The definitions of the mechanical components of the system are shown in Fig. 3A and consist of: 1) the servo-controlled displacement of the load point u_o, 2) the machine stiffness k_m, 3) the displacement of the shear box u_{box}, 4) the sample assembly stiffness k_{fb}, which is the stiffness between the measuring points on the box and the fault, thus integrating the components of the box, cement, rock and surface geometry, and 5) the displacement of the fault u_f.

The machine stiffness k_m is obtained by two independent methods during controlled loading and instantaneous unloading segments within stick-slip cycles, after total shear displacement has exceeded at least 4 mm. Consider Fig. 3B where a sequence of three stick-slip cycles measured for the Sawcut interface is plotted. The reloading slopes, denoted here as k_i, are obtained from controlled loading under prescribed load point displacement rate

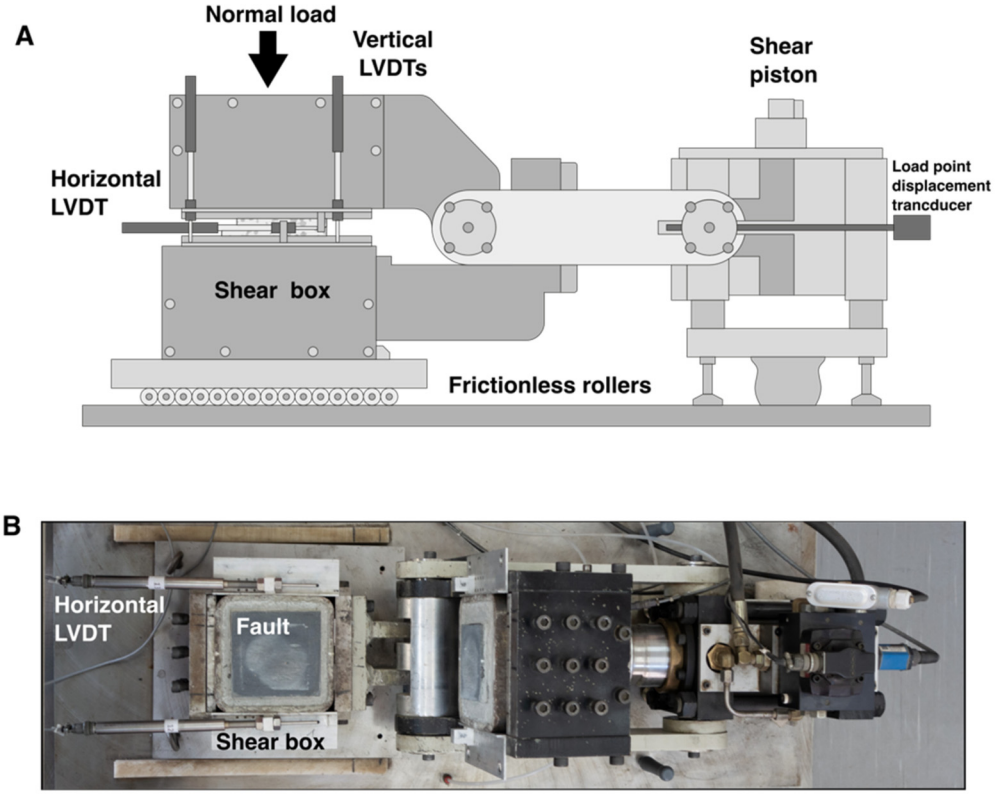

Fig. 2. A) Schematic illustration of the direct shear system used in this research. The frame of the horizontal shear actuator is coupled to the upper sample holder frame via two plates (the near one shown in light grey) and two circular shafts with bearings. Not shown, the piston of the horizontal shear actuator is attached to the shear box frame via the shear load cell. Relative block displacement is monitored by two horizontal LVDTs (one of which is shown) mounted on the shear box close to the sliding interface. Vertical displacement through shear is monitored by four LVDTs (two of which are shown). B) Top view of the shear box and the tested interface. Note the sample stack assembly between the horizontal LVDTs and the tested interface.

during stick phases, whereas the unloading slopes (denoted k_m) are obtained instantaneously during slip phases. During controlled loading segments the difference between the load point and shear box displacement can be used to recover k_m:

$$k_{\mathrm{m}(loading)} = \frac{\Delta F_{loading}}{(u_{loadpoint} - u_{box})}, \tag{2}$$

where $\Delta F_{\ loading}$ is the shear force difference during a loading segment and $u_{load\ point}$ and u_{box} are the displacement of the shear piston and shear box, respectively (see Fig. 3D). Moreover, from the theoretical solution for stick-slip oscillations under constant load point displacement rate (Jaeger et al., 2007), the slopes of the instantaneous unloading segments during slip phases also provide k_m:

$$k_{\mathrm{m}(unloading)} = \frac{\Delta F_{unloding}}{\Delta u_{box}}, \tag{3}$$

where Δu_{box} is the displacement from the beginning of the current slip event to its end as measured from the horizontal LVDTs. Both methods return strikingly similar k_m values of 10^5 N/mm or 10.8 MPa/mm, regardless of the interface roughness (Fig. 3E).

4.2. Calculation of stick and slip velocities

We measure the stick velocity (v_{stick}) from the slope of horizontal displacement vs. time curve within a stick cycle (Fig. 3C). Because of non-linearity towards the end of each segment (see Fig. 3B), each measurement is taken between initial reloading point up to 50% of the level of shear stress rise within the segment. In order to obtain the slip velocity (v_{slip}) we use the acquired data points within a slip cycle (typically 5 points due to the short event duration and the data acquisition rate of 50 Hz) and find the two data points between which the horizontal displacement is highest. We then take the slope between that point and the two adjoining points above and below to calculate the slip velocity in that cycle (see inset in Fig. 3C). It is important to note that even though our measurement resolution is relatively low considering the short duration of the slip events, the three-point slopes return strikingly similar values between slip segments. It must be pointed out here that all velocities computed by us refer to the shear box velocities as obtained by the horizontal LVDTs outputs, and not to the fault velocities.

4.3. Calculation of the shear stiffness

The concept of shear stiffness of an interface tested in direct shear, denoted here k_i, is often used in the experimental rock mechanics literature and is defined as (Goodman, 1989): $k_i = \frac{\Delta\tau}{\Delta u_{box}}$. It can be appreciated from inspection of Fig. 3B that the slope of the reloading curve is not linear from beginning to end, and therefore the value of k_i is calculated for the linear segment of the reloading curve, from 0 up to 50% increase in shear stress, as in the calculation of v_{stick} discussed above.

It is instructive to examine the relationship between the shear stiffness defined above (k_i) and the other stiffnesses involved in the mechanical testing system. As illustrated in Fig. 3A, the effective stiffness of the system k_s including both the shear load frame k_m and the sample assembly stiffness k_{fb} is the sum of the compliances that are the reciprocal of the stiffnesses, namely:

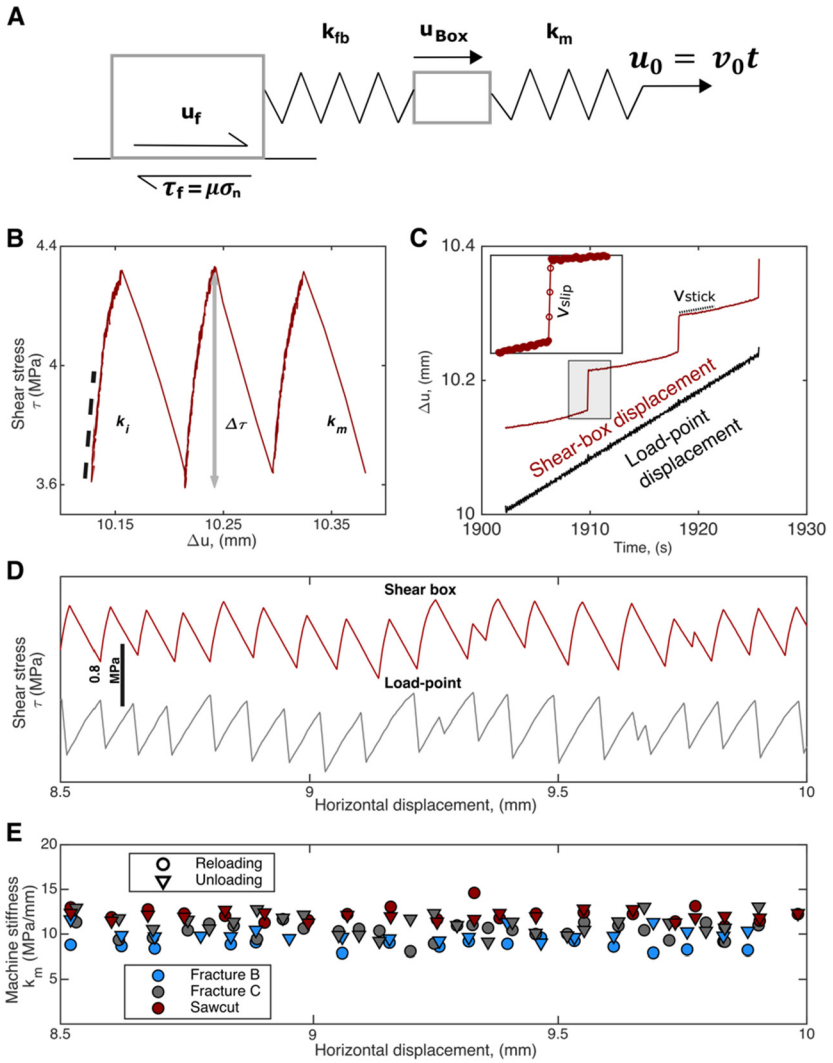

Fig. 3. Experimental measurement of relevant quantities. A) Schematic illustration of the mechanical components of the system, B) Shear stress vs. displacement during three stick-slip oscillations on a sawcut interface and the experimental method to obtain k_i and k_m, C) Displacement vs. time for the same oscillations as in B showing the procedure to obtain v_{stick} and v_{slip}, D) Example of shear box vs. shear piston (load point) displacement during stick-slip oscillations. The difference between these two outputs during reloading segments is used to calculate the machine stiffness k_m, and the unloading curves of the load-point displacement are used to obtain k_m from the instantaneous unloading (slip) segments, E) Machine stiffness k_m calculated from stick-slip oscillations during both loading (stick) and unloading (slip) segments, measured for Fracture B, C and Sawcut interfaces between 8.5 - 10 mm of displacement. Note the similarity between the results obtained for the three interfaces using the two independent measurement methods.

$k_s = \frac{1}{(\frac{1}{k_{fb}} + \frac{1}{k_m})}$. Considering the linear segment of a stick-slip cycle, the force balance during this stage is:

$$\Delta\tau = k_{fb}(\Delta u_{box} - \Delta u_f) = k_{fb}(v_{box,stick}\Delta t - v_{f,stick}\Delta t), \quad (4)$$

and also

$$\Delta\tau = k_i \Delta u_{box} = k_i v_{box,stick}\Delta t, \quad (5)$$

where here we distinguish between the velocities of the box and of the fault during the stick segments. In the rest of the paper the designation "box" in connection with velocities and displacements is not always used, therefore whenever v_{stick} and v_{slip} are discussed the meaning is for box velocities, unless indicated otherwise. Similarly with respect to displacements, whenever Δu or the term "shear displacement" are indicated we typically refer to box displacement, unless indicated otherwise. Equating equations (4) and (5) and dividing by Δt:

$$k_i v_{box,stick} = k_{fb}(v_{box,stick} - v_{f,stick}), \quad (6)$$

thus, and strictly for loading segments, the sample assembly stiffness is:

$$k_{fb} = k_i \frac{v_{box,stick}}{v_{box,stick} - v_{f,stick}}, \quad (7)$$

This derivation implies that k_{fb} can only be equal to k_i (assuming linearity) during a loading cycle if the velocity of the fault during a stick segment is zero. In our testing configuration we do not have a direct constraint on $v_{f,stick}$, but we do not think that $v_{f,stick}$ can be zero during loading cycles. Considering the rigidity of the cement and the sample stack between the LVDTs and the fault and assuming linear elasticity, we estimate that at least 90% of the horizontal displacement measured by the LVDTs derives from slip across the fault and the rest from elastic distortions of materials in the sample stack between the LVDTs and the fault, primarily the cement in which the fault is embedded. Because we do not have a rigorous constraint on $v_{f,stick}$ we cannot resolve the exact magnitude of k_{fb} and consequently of k_s, but for $v_{f,stick} \geq 0.9 v_{box,stick}$ (if 90% of the slip is on the fault), we can estimate from eq. (7) that $k_{fb} \geq 10 k_i$.

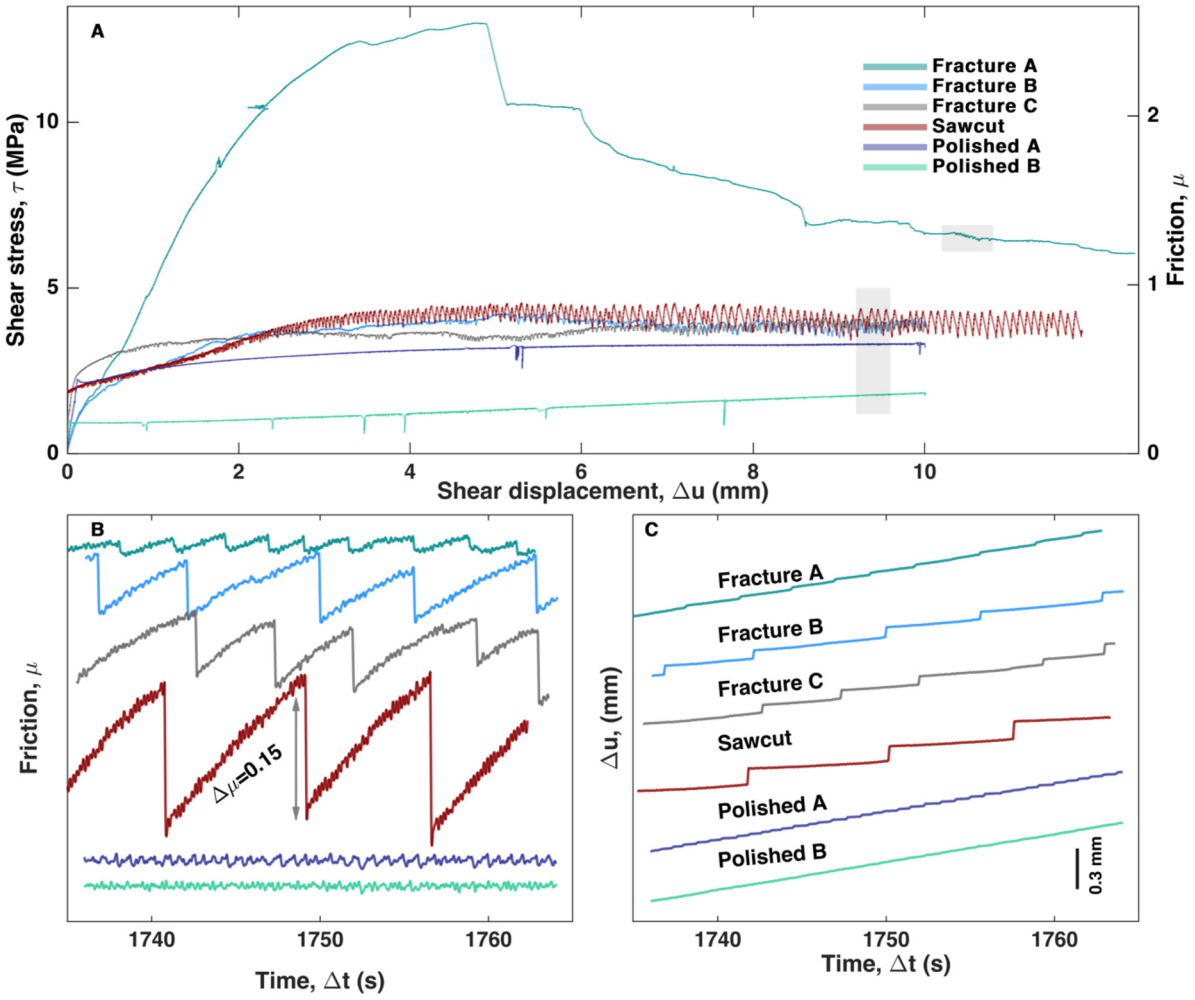

Fig. 4. A) Shear stress vs. shear displacement for six levels of initial fault roughness. Changes in friction coefficient (B) and shear displacement (C) in all faults (grey areas in A) as a function of time. Maximum oscillation amplitude is measured for the sawcut surface, decreasing for both smoother and rougher surfaces.

5. Results

The experimental results present a wide spectrum of mechanical behaviours and slip dynamics, ranging from stick-slip to stable sliding (Fig. 4A). Detailed plots of friction (τ/σ_n) vs. displacement and time are shown in Fig. 4B and C, respectively. The Sawcut interface produces the most pronounced stick slip events, where the events do not start immediately with onset of sliding, but rather, following a preceding stage in which shear stress gradually increases with slip to a value of ~4 MPa. The moderately rough Fractures (B, C) show similar behaviour but with less regular stick-slip events and smaller stress oscillations.

The amplitude of the stick slip events diminishes towards the two roughness extremes. The roughest sample (Fracture A) exhibits brittle fracture followed by mostly stable sliding where the shear stress gradually increases to a peak value of ~13 MPa, followed by a major stress drop of ~3 MPa, and then by a gradual decrease with slip (Fig. 4A). Brief oscillatory stick-slip episodes are observed at slip distance larger than 10 mm (shaded grey area in Fracture A curve). Visual inspection of the sample after the experiment reveals combined off-fault fracturing coupled with frictional slip across the pre-existing surface. The smoothest samples (Polished A, B) slide in a relatively stable manner. The slightly smoother Polished B surface exhibits a local peak friction of 0.18 followed by stable sliding with moderate slip hardening (Fig. 4A). The obtained friction is extremely low comparing to measurements in previous experiments performed on similar rocks under similar loading conditions (Marone and Cox, 1994; Yamashita et al., 2018). The slightly rougher Polished A surface exhibits similar characteristics but with higher friction, more moderate slip hardening, and less stable slip, expressed by stress undulations with amplitudes close to our detection level (Figs. 4B, C).

We further investigate the stick-slip characteristics at the four experiments where the phenomena is clearly present. The Sawcut interface, which is the most prone to stick slip deformation, exhibits the slowest stick velocity ($v_{stick} = 0.003$ mm/s) and highest slip velocity, with peak values of $v_{slip} = 1$ mm/s (Figs. 5A, 5B). Correspondingly, it shows the highest values of shear stiffness (k_i) as calculated during the stick phases, with average value of 34.5 MPa/mm (Fig. 5C), and largest stress drops ($\Delta\tau$) during the slip events with values of 0.7–0.8 MPa at slip distance larger than 7 mm (Fig. 5D). The values of $\Delta\tau$, v_{slip}, and k_i decrease significantly with increasing roughness levels. Interestingly, the parameters k_i and v_{stick} associated with the stick segments remain relatively constant for a given roughness throughout shear displacement (Figs. 5A, 5C), whereas the parameters $\Delta\tau$ and v_{slip} associated with slip segments generally increase with cumulative slip, Δu (Figs. 5B and 5D).

To this end, we have shown strong dependency between fault roughness and slip dynamics, where stick slip oscillations are found to be constrained to a distinct surface roughness range. Further experiments on fault surface "Polished A" show that the geometrical evolution of the surface is also critical to slip dynam-

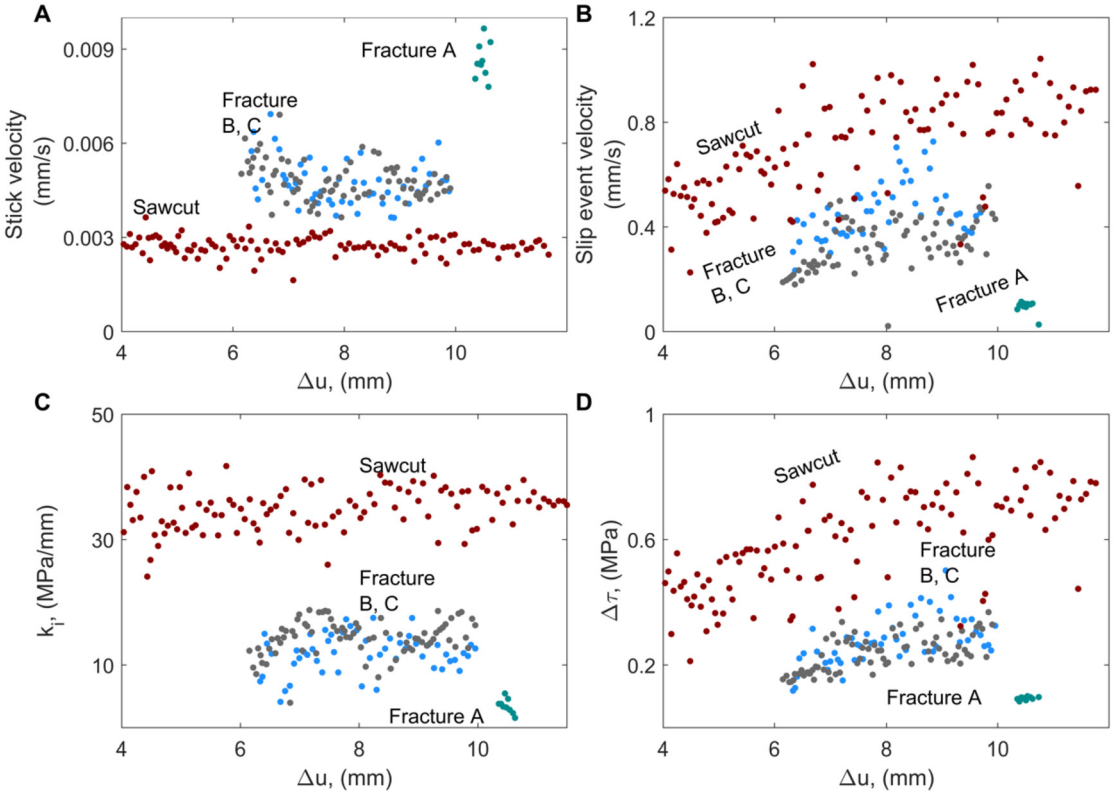

Fig. 5. Characteristics of stick slip oscillations for different initial fault roughness. A) Sliding velocity during stick segment vs. shear displacement, B) Sliding velocity during slip events vs. shear displacement, C) Variations in shear stiffness k_i as a function of fault roughness, D) Variations in stress drop $\Delta\tau$ as a function of fault roughness.

ics. This surface exhibited relatively stable sliding during the first experiment (Fig. 4). At a later experiment on this same interface, that started in a velocity stepping sequence where the induced velocity is changed after prescribed displacement targets to prescribed values, followed by shear at a constant rate of 0.01 mm/s, the surface exhibited transition to stick slip oscillations, with average stress drop $\Delta\tau$ and shear stiffness k_i values of 0.11 MPa and 23 MPa/mm, respectively (Fig. 6A). A plot of the initial roughness of the Polished A and Sawcut surfaces together with the roughness measured after the velocity stepping sequence performed on the Polished A fault (inset in Fig. 6A) shows that the detected stick slip instability is clearly associated with roughening of the evolved surface. Moreover, detailed visual examination of Polished A fault surface demonstrates that the roughening is expressed by discrete zones of high geometrical variations, mostly protruding along profiles measured perpendicular to the slip direction (Fig. 6B).

The average values of shear stiffness and stress drop as a function of initial fault roughness are plotted in Fig. 7. Because surface Polished B exhibited stable sliding during the entire run, we were not able to measure its shear stiffness. The most significant result we report here is that sliding instability, as manifested by the magnitude of the stress drops during stick slip cycles, clearly peaks for a very distinct roughness value, with decreasing stress drops measured both for the rougher and the smoother surfaces. We define the roughness associated with peak stress drop during stick slip oscillations as the *critical roughness* of the fault surface for the given boundary conditions.

6. Discussion

6.1. Shear stiffness vs. critical stiffness

The stability of frictional systems is generally explained by the interplay between the effective system stiffness (k_s) and the critical stiffness of the interface (k_c) (Rabinowicz, 1958; Rice and Ruina, 1983; Ruina, 1983). The critical stiffness k_c is typically calculated from measured rate and state (RS) (Dieterich, 1979; Ruina, 1983) friction parameters (A, B, d_c) as: $k_c = \sigma(A-B)/d_c$, (Ruina, 1983). The RS parameters are challenging to obtain experimentally during unstable sliding, especially for the range of roughnesses in our study. Let us examine how k_s varies between the experiments. In section 4.3, we obtained that $k_{fb} \geq 10k_i$, recalling that k_{fb} is the sample assembly stiffness and k_i is the shear stiffness. Together with the observation that for the Polished A, Sawcut and Fractured B and C surfaces, $k_i \geq k_m \sim 10$ MPa/mm (Fig. 7) that gives $k_{fb} \geq 10k_m$, recalling that k_m is the machine stiffness. Substituting in the expression for the effective stiffness in our system of two springs in series (Fig. 3A), we obtain $k_s = \frac{1}{(\frac{1}{k_{fb}}+\frac{1}{k_m})} \approx k_m$. Therefore, although the roughness affects the stiffness k_{fb} (Dieterich and Smith, 2009; Fang and Dunham, 2013), its influence on k_s in our experimental setup is negligible. This suggests that the effective system stiffness k_s barely varies between the experiments, thus the increased stability from the Sawcut to the Fractured and Polished surfaces appears to be associated with a decrease in the critical stiffness k_c.

While the discussion above focuses on the development of frictional instability during slip phases, we can examine the tendency of the surfaces to experience stick-slip behaviour using the shear stiffness, k_i, as measured at $\Delta u > 4$ mm, which represents the resistance of the interface to shear during the stick segments and, in contrast to k_c, can be measured directly when stick-slip behaviour is presented (Figs. 5C, 6A). We suggest that the larger k_i values for the Sawcut interface (Fig. 7) correspond to a larger shear resistance during loading segments, which leads to a more efficient locking and consequently lower stick velocity (Fig. 5A) and larger accumulation of elastic strain energy during the loading segments, consequently leading to more intense slip events

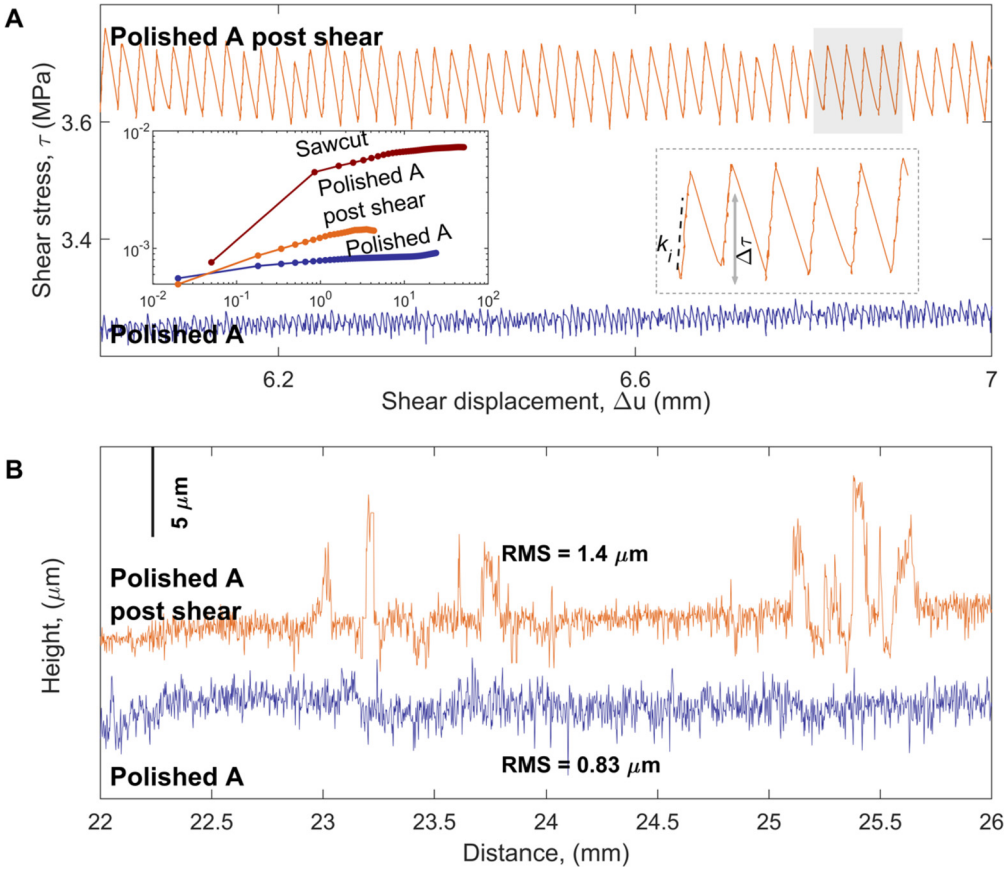

Fig. 6. A) Steady state sliding before (blue) and after (orange) a sequence of velocity stepping experiments was performed on the Polished A fault, B) 2D profiles of Polished A fault surface before (blue) and after (orange) shear, scanned perpendicular to the shear direction with vertical exaggeration of X 400. (For interpretation of the colours in the figure(s), the reader is referred to the web version of this article.)

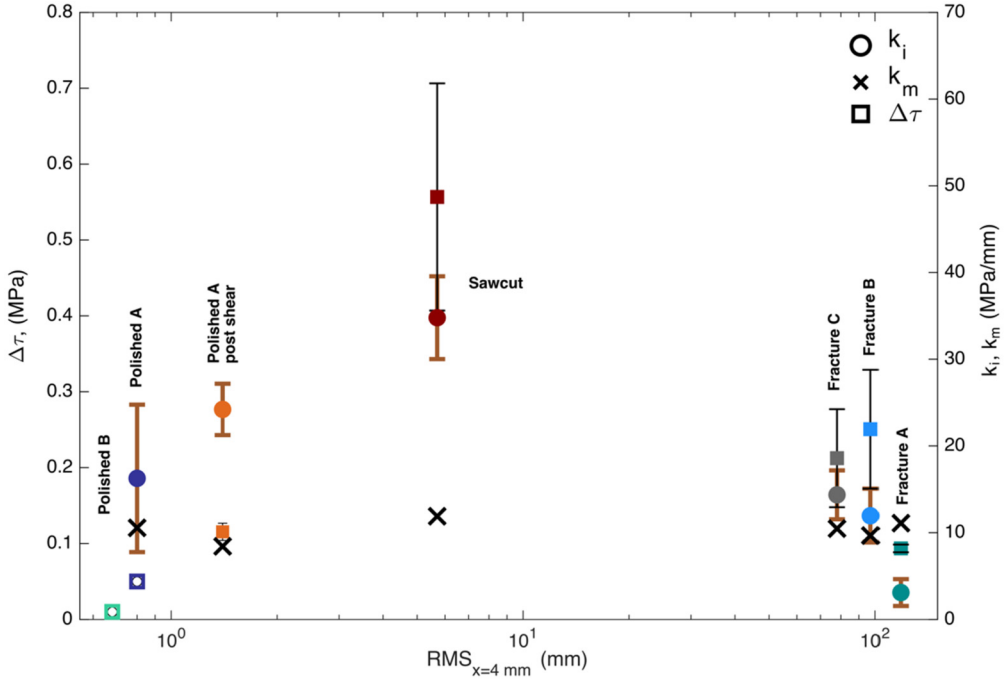

Fig. 7. Stick slip oscillations peak at a critical roughness: The average magnitudes of stress drop $\Delta\tau$, shear stiffness k_i, and machine stiffness k_m for each level of initial fault roughness. The RMS values reported in this plot are for profile sampling length of 4 mm for all surfaces, which is also equal to the initial displacement from which we measured the stick slip parameters. Different sampling length would change the scale of the x-axis but not the general behaviour because the RMS curves do not cross each other at any sampling length (Fig. 1D). Empty boxes represent estimated value as the magnitude of stress drop is near the detection resolution of the shear load cell.

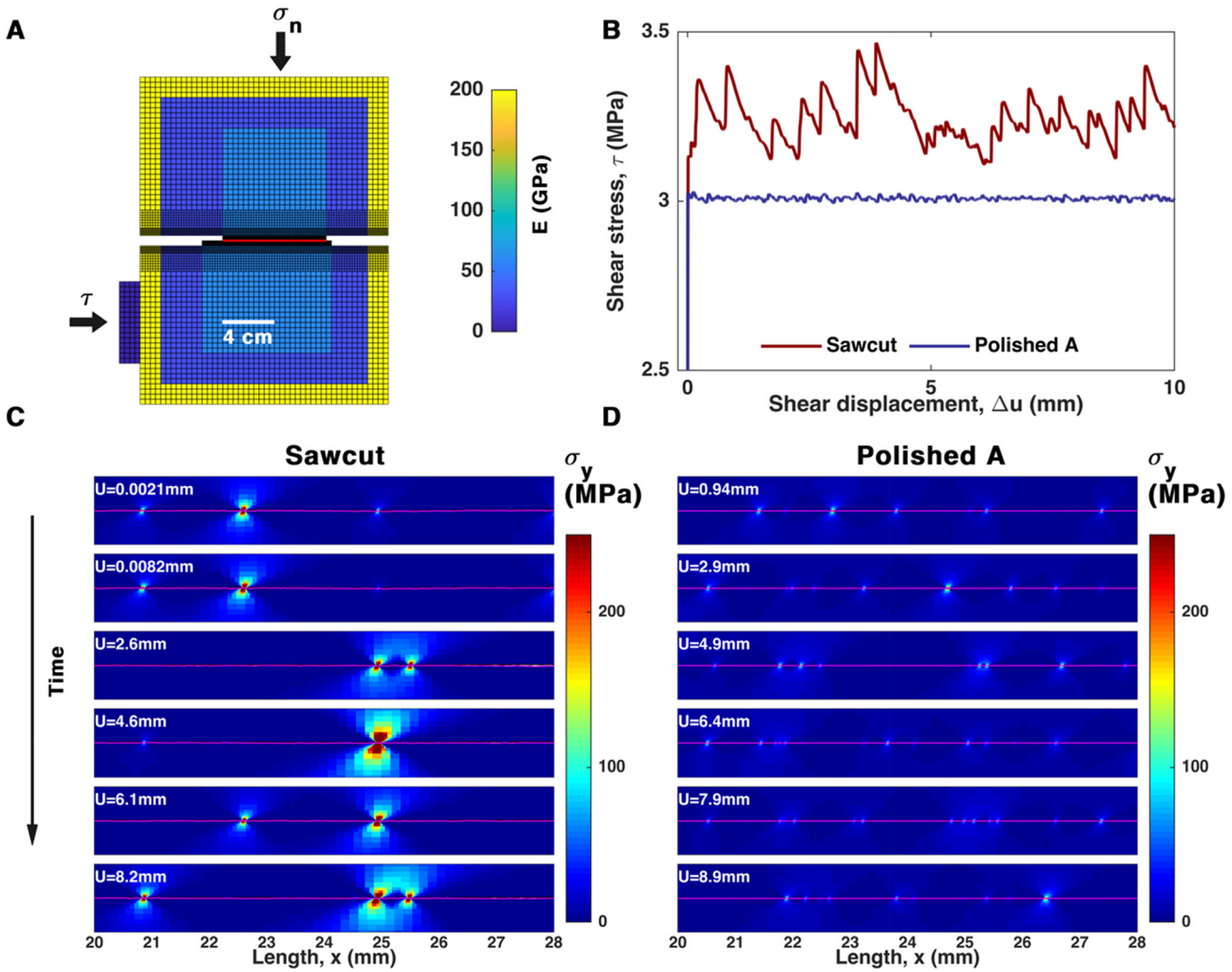

Fig. 8. Numerical FEM simulations show that a minimum level of roughness is important for stick slip behaviour: A) the modelled shear box in the FEM model, B) Shear stress vs shear displacement for the modelled Polished A and Sawcut interfaces, C) normal stress evolution with shear displacement near an 8 mm segment of the Sawcut fault surface, D) normal stress evolution with shear displacement near an 8 mm segment of the Polished A fault surface. Note that while scale is limited to 250 MPa for better visualization, the stresses on some of the asperity contacts on the Sawcut interface exceed 1000 MPa.

with larger stress drops (Fig. 7) and sliding velocity (Fig. 5B). The lower k_i values of the fractured interfaces imply less efficient locking during the loading segments and consequently lead to smaller slip events. The mechanism that governs the reduction in k_i with increasing roughness may be related to enhanced stress concentrations around steep asperities (e.g. Sagy and Lyakhovsky, 2019) that might lead to inelastic flow or to decreasing asperity nucleation length, as discussed by Aubry et al. (2020). Similar interpretations of the effects of stress heterogeneity on slip stability have been developed from field observations of slip behaviour on large scale fault zones (e.g. Barcheck et al., 2021).

The increased stability of sliding with decreasing roughness, as evident from the transition from the Sawcut to the Polished fault interfaces (Fig. 7) suggests, on the other hand, that a minimum level of roughness is required for efficient mechanical interlocking of asperity contacts. Otherwise, the local stresses at the contacts are not large enough to prevent continuous stable sliding of the interface.

We test this hypothesis with numerical quasistatic simulations of the shear experiments on the Sawcut and Polished A interfaces (Fig. 8), using a finite element code that allows large sliding across rough interfaces (Tal et al., 2020; Tal and Hager, 2018). Moreover, the simulations enable us to get more insight on evolution of the local contacts and stresses on the fault, which cannot be observed in the experiments. Boundary conditions and elastic properties in the model were similar to those in the experiments (Fig. 8A), with the latter representing the sample, cement, and shear boxes, as well as the machine stiffness, which is represented by the soft elements at the lower left part of the model. The modelled interfaces were generated using the roughness measurements of the experimental interfaces in the direction parallel to slip (Fig. 1), accounting for wavelengths larger than ~0.1 mm. Although the numerical code allows different friction formulations and plastic off-fault deformation, we set a constant nominal friction coefficient value of $\mu = 0.6$ and account only for elastic deformation to isolate the mechanical effect of fault geometry.

Remarkably, while the modelled Polished A fault surface slides stably, the roughness of the modelled Sawcut fault surface induces stick slip, despite the constant friction coefficient and elastic rheology of the contacts (Fig. 8B). Inspection of the normal stress evolution across an 8 mm long segments of the two modelled fault surfaces (Figs. 8 C, D) reveals how the contacts evolve with slip as different asperities become at contact. The modelled Sawcut surface has 2 – 3 asperity contacts with high stress concentrations along the segment (Fig. 8C), while the modelled Polished A surface has 7 – 12 asperity contacts, each with a significantly lower stress. (Fig. 8D). The model suggests that geometrical interlocking of asperities with development of large local stresses is a key pro-

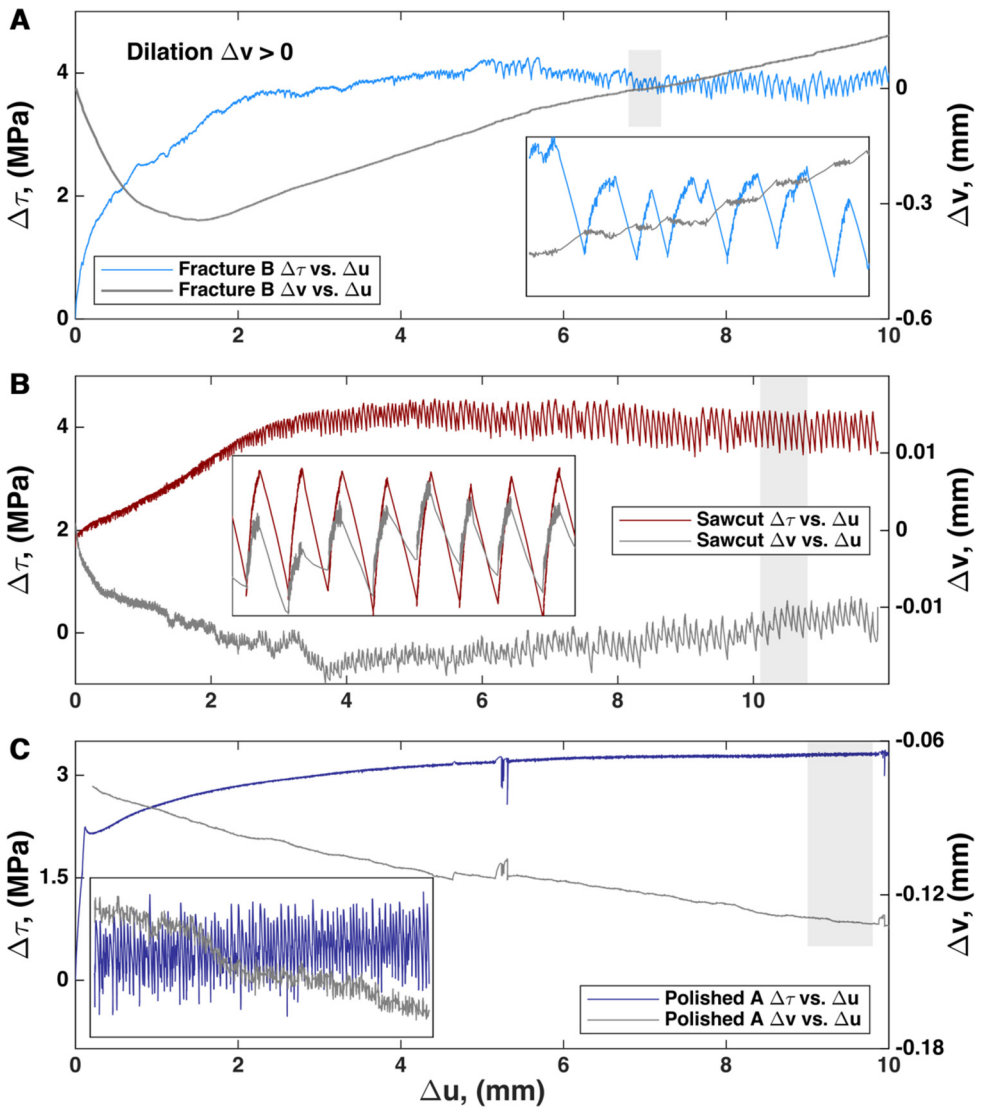

Fig. 9. Evolution of shear stress ($\Delta\tau$) and dilation (ΔV) through shear across Fracture B (A), Sawcut (B), and Polished A (C) fault surfaces as a function of shear displacement (Δu). Location of insets shown in grey boxes. Note here dilation is positive.

cess in stick slip behaviour of bare surfaces. Moreover, as per the mathematical definition of the critical stiffness k_c above, enhanced normal stress concentrations would lead to higher critical stiffness of the sawcut prompting less stable sliding per a given effective system stiffness k_s. We note that the stick slip behaviour in the model is less regular and with smaller stress drops than in the experiment and suggest that the mechanical interlocking in the experiments enhances other micro mechanical and frictional processes that promote instability and are not accounted for in the model.

6.2. Probing into dilation through shear

An important insight concerning the micromechanics of sliding instabilities can be gained from inspection of the dilatant behaviour of the different fault surfaces during shear under constant normal stress. Consider Fig. 9 where the dilatant behaviour of the Fracture B, Sawcut, and Polished A fault surfaces are plotted vs. shear displacement Δu, for the entire 10 mm slip. All faults undergo some contraction at the initial stages of the tests indicated by negative output of the vertical LVDT. The dilatant behaviour after ultimate shear resistance is reached however varies drastically between the fault surfaces. The relatively rough Fracture B fault (Fig. 9A) exhibits significant dilation through shear at the macro scale, yet within stick – slip cycles (shaded box and inset) the samples do not dilate during stick segments where most of the dilation is accommodated during the dynamic slip events. Such a behaviour may indicate temporary interlocking of the interface during stick phases. In contrast, the Sawcut fault (Fig. 9B) does not exhibit dilation through shear at the macro scale, yet when examining the dilatant behaviour during stick-slip cycles at the micro scale (see inset) a clear coupling between stick slip oscillations is observed, where the dilation and stick slip oscillations appear to be completely in phase. The unique observation shown in Fig. 9B suggests that under the normal stresses applied in our experiments, the governing micro mechanism during stick-slip deformation of faults with surfaces exhibiting critical roughness, is overriding over asperity contacts rather than shearing through them. Faults that are rougher than critical exhibit predominantly a mechanism of shearing through asperities (inset in Fig. 9A) whereas slip across faults that are smoother from critical is completely decoupled from dilation (inset in Fig. 9C). It should be pointed out that compaction / dilation trends have been reported in experiments performed on granular materials, where similar micromechanical interpretations can be inferred and transitions from overriding to shearing through

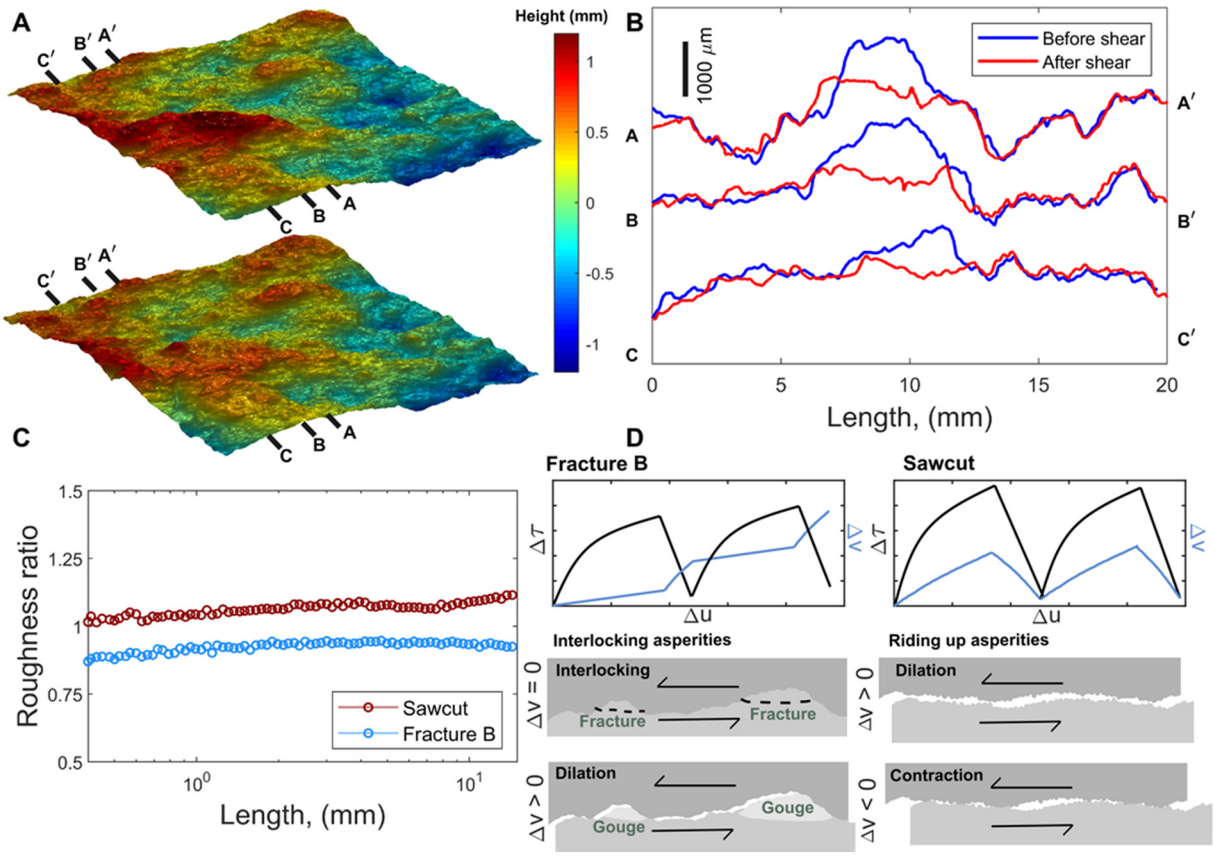

Fig. 10. Micromechanics of dilatant shear. A) Topographic map of Fracture B fault surface with location of three cross sections (B) performed before (upper) and after (lower) shear, C) The evolution of RMS Ratio$_{(x)}$ for the Sawcut and Fracture B fault surfaces, D) A schematic micromechanical model for shear through faults exhibiting critical (Sawcut) and rougher than critical (Fracture B) roughness.

can be observed with progressive grain size reduction / breakage (e.g. Fulton and Rathbun, 2011).

A good demonstration of the "shearing through" mechanism argued by us to be dominant in the rougher-than-critical fault surfaces is obtained from cross sections performed through the Fracture B surface, in parallel to the slip direction, before and after shear (Fig. 10A). In all three cross sections the protruding asperities are clearly truncated through shear (Fig. 10B). In contrast, shear through the Sawcut fault surface is dominated by a strongly dilatant "gliding over" mechanism that can be appreciated when comparing the roughness before and after shear through the "RMS Ratio$_{(x)}$" defined as: $RMS\ Ratio_{(x)} = Final\ RMS_{(x)}/Initial\ RMS_{(x)}$ (Fig. 10C), where x is the length in the shear direction. It can be clearly appreciated that the RMS Ratio$_{(x)}$ of Fracture B is <1 and therefore reflecting smoothing, as displayed similarly for specific profiles in Fig. 10B. The Sawcut sample is mostly unaffected, as indicated RMS Ratio$_{(x)}$ values close to 1. A schematic illustration demonstrating this micromechanical model is shown in Fig. 10D. The general intense dilatancy of the Fracture B sample at the macroscale (Fig. 9A) is now understood in terms of asperity fracture, wear production and accumulation. This process is less dominant in the Sawcut sample where at the microscale the dilation is in phase with the stick slip oscillations but overall, at the macroscale, that sample does not dilate through shear (Fig. 9B) as also evident by less roughness variations before and after shear (Fig. 10C).

6.3. Implications to natural slip phenomena

The present series of experiments demonstrates the influence of surface roughness on slip dynamics and resistance to shear, as follows: 1) Stable sliding for the extremely smooth surfaces (Polished A, B), 2) Oscillatory stick slips for the rough surfaces (Fracture B, C, Sawcut), and 3) Distinct peak stress and high stress-drop associated with off-fault fracturing followed by stable sliding, for the roughest surface (Fracture A). These findings are of paramount importance for earthquake nucleation, catastrophic landslide initiation, glacier sliding, and discontinuous rock instabilities in general. While dynamic effects and co-seismic weakening of friction enable ruptures to propagate on frictionally stable fault segments (Noda and Lapusta, 2013), the nucleation phase is limited to segments where the frictional and loading conditions allow the development of frictional instability. Our laboratory results indicate that, in addition to normal stress and fault zone material, the roughness level is a key parameter in the development of such instabilities.

The analogy between stick-slip frictional sliding at laboratory experiments and natural earthquakes has long been recognized (Brace and Byerlee, 1966). As our experiments are performed under a relatively low normal stress, they are more relevant to shallow phenomena, and might explain seismic records that are interpreted as stick slip events prior to large landslides (Yamada et al., 2016), as well as the occurrence of stick slip behaviour during movement of glaciers and ice sheets across the contact between ice and bedrock (e.g. Fischer and Clarke, 1997).

Recent rock mechanics experiments show that roughness controls slip instability also under much higher stresses corresponding to seismic depths (e.g. Aubry et al., 2020; Dresen et al., 2020; Harbord et al., 2017), and although the range of roughness profiles studied in these works is much narrower than studied here, the relevance of our results might be extended to natural faulting. Indeed, several seismological and geophysical observations of large thrust faults suggest that fault geometry affects earthquake char-

acteristics (e.g. Wang and Bilek, 2011), yet the exact effects are currently being debated (e.g. Mochizuki et al., 2008). Our experiments clearly demonstrate that there exists a specific geometry that enhances sliding instability. We suggest that the stick-slip instability magnitudes increase when the local barriers along natural slip surfaces allow efficient locking and accumulation of energy during the inter-seismic stage, without increased stress concentrations that lead to inelastic flow. This occurs in our experiments at a specific roughness level, corresponding the Sawcut surface.

7. Conclusions

The reported non-linear dependency of stick slip oscillations on surface roughness (Fig. 4, 7) is unique. We show that there exists a critical fault roughness with rougher or smoother fault surfaces exhibiting more stable sliding. The decreasing stress drop and slip stabilization associated with the transition from critical to higher roughness levels is in agreement with previous studies (Harbord et al., 2017; Okubo and Dieterich, 1984; Yamashita et al., 2018), although we consider here a significantly wider spectrum of roughness levels. However, the gradual stabilization from critical to extremely smooth fault roughness is a new discovery, reported here for the first time for such a large span of roughness profiles. By probing into the dilatant response of the sheared interfaces we show that shear across fault surfaces of critical roughness (here these are the Sawcut surfaces) is completely coupled with the stick slip oscillations, namely the dilation and stick slip motions are in phase, and indeed comparison of the roughness before and after slip of these surfaces reveals that the roughness ratio remains largely the same. Shearing of faults with roughness smaller than critical is typically characterised by stable sliding and indeed numerical modelling with FEM show that the normal stress intensities at asperity tips clearly diminish for slip across very smooth interfaces, indicating less effective interlocking. The decreasing level of normal stress, as well as the similar system stiffness in the experiments, imply that the stabilization is associated with a decrease in the critical stiffness (k_c). In addition, we suggest that the readily measurable shear stiffness (k_i), which determines the locking efficiency during the stick phases, can be used to assess the tendency of a tested fault surface to exhibit sliding instability.

CRediT authorship contribution statement

Doron Morad: Conceptualization, Formal analysis, Investigation, Methodology, Software, Visualization, Writing – original draft. **Amir Sagy:** Conceptualization, Formal analysis, Funding acquisition, Resources, Supervision, Writing – review & editing. **Yuval Tal:** Formal analysis, Resources, Software, Writing – review & editing. **Yossef H. Hatzor:** Conceptualization, Funding acquisition, Investigation, Methodology, Project administration, Resources, Supervision, Writing – review & editing.

Declaration of competing interest

The authors declare that they have no known competing financial interests or personal relationships that could have appeared to influence the work reported in this paper.

Acknowledgements

This research is funded by Israel Science Foundation (ISF) through contract no. 937/17. We thank Gil Cohen for help with the white light interferometer. We thank Patrick Fulton and Cheng Mei for critically reviewing the paper and for their constructive and insightful comments.

References

Archard, J.F., 1957. Elastic deformation and the laws of friction. Proc. R. Soc. Lond., Ser. A, Math. Phys. Eng. Sci. 243, 190–205.
Aubry, J., Passelegue, F.X., Escartin, J., Gasc, J., Deldicque, D., Schubnel, A., 2020. Fault stability across the seismogenic zone. J. Geophys. Res., Solid Earth 125 (8).
Badt, N., Hatzor, Y.H., Toussaint, R., Sagy, A., 2016. Geometrical evolution of interlocked rough slip surfaces: the role of normal stress. Earth Planet. Sci. Lett. 443, 153–161.
Barcheck, G., Brodsky, E.E., Fulton, P.M., King, M.A., Siegfried, M.R., Tulaczyk, S., 2021. Migratory earthquake precursors are dominant on an ice stream fault. Sci. Adv. 7 (6).
Biran, O., Hatzor, Y.H., Ziv, A., 2009. Micro-scale roughness effects on the friction coefficient of granite surfaces under varying levels of normal stress. In: Hatzor, Y., Sulem, J., Vardoulakis, I. (Eds.), Shear Physics at the Meso-Scale in Earthquake and Landslide Mechanics. CRC Press/Balkema, The Netherlands, pp. 145–158.
Bowden, F., Tabor, D., 1950. The Friction and Lubrication of Solids. Oxford University Press.
Brace, W.F., Byerlee, J.D., 1966. Stick-slip as a mechanism for earthquakes. Science 153 (3739), 990–992.
Brantut, N., 2020. Dilatancy-induced fluid pressure drop during dynamic rupture: direct experimental evidence and consequences for earthquake dynamics. Earth Planet. Sci. Lett. 538, 10.
Byerlee, J., 1978. Friction of rocks. Pure Appl. Geophys. 116 (4-5), 615–626.
Candela, T., Renard, F., Klinger, Y., Mair, K., Schmittbuhl, J., Brodsky, E.E., 2012. Roughness of fault surfaces over nine decades of length scales. J. Geophys. Res., Solid Earth 117.
Dieterich, J.H., 1979. Modeling of rock friction. 1. Experimental results and constitutive equations. J. Geophys. Res. 84, 2161–2168.
Dieterich, J.H., Kilgore, B.D., 1994. Direct observation of frictional contacts - new insights for state-dependent properties. Pure Appl. Geophys. 143 (1–3), 283–302.
Dieterich, J.H., Smith, D.E., 2009. Nonplanar faults: mechanics of slip and off-fault damage. Pure Appl. Geophys. 166 (10-11), 1799–1815.
Dresen, G., Kwiatek, G., Goebel, T., Ben-Zion, Y., 2020. Seismic and aseismic preparatory processes before large stick-slip failure. Pure Appl. Geophys. 177 (12), 5741–5760.
Fan, X.M., Xu, Q., Scaringi, G., Dai, L.X., Li, W.L., Dong, X.J., Zhu, X., Pei, X.J., Dai, K.R., Havenith, H.B., 2017. Failure mechanism and kinematics of the deadly June 24th 2017 Xinmo landslide, Maoxian, Sichuan, China. Landslides 14 (6), 2129–2146.
Fang, Y., Elsworth, D., Wang, C.Y., Ishibashi, T., Fitts, J.P., 2017. Frictional stability-permeability relationships for fractures in shales. J. Geophys. Res., Solid Earth 122 (3), 1760–1776.
Fang, Z.J., Dunham, E.M., 2013. Additional shear resistance from fault roughness and stress levels on geometrically complex faults. J. Geophys. Res., Solid Earth 118 (7), 3642–3654.
Fischer, U.H., Clarke, G.K.C., 1997. Stick-slip sliding behaviour at the base of a glacier. In: Proceedings International Symposium on Changing Glaciers, vol. 24. Fjaerland, Norway, Jun 24-27 1996, pp. 390–396.
Fulton, P.M., Rathbun, A.P., 2011. Experimental constraints on energy partitioning during stick-slip and stable sliding within analog fault gouge. Earth Planet. Sci. Lett. 308 (1–2), 185–192.
Goebel, T.H.W., Kwiatek, G., Becker, T.W., Brodsky, E.E., Dresen, G., 2017. What allows seismic events to grow big?: insights from b-value and fault roughness analysis in laboratory stick-slip experiments. Geology 45 (9), 815–818.
Goodman, R.E., 1989. Introduction to Rock Mechanics. John Wiley & Sons, New York. 562 p.
Gordin, Y., Hatzor, Y.H., Vinegar, H.J., 2020. Anisotropy evolution during early maturation of organic-rich carbonates. J. Pet. Sci. Eng. 188.
Gupta, H.K., 2002. A review of recent studies of triggered earthquakes by artificial water reservoirs with special emphasis on earthquakes in Koyna, India. Earth-Sci. Rev. 58 (3-4), 279–310.
Harbord, C.W.A., Nielsen, S.B., De Paola, N., Holdsworth, R.E., 2017. Earthquake nucleation on rough faults. Geology 45 (10), 931–934.
Ibanez, J.P., Hatzor, Y.H., 2018. Rapid sliding and friction degradation: lessons from the catastrophic Vajont landslide. Eng. Geol. 244, 96–106.
Jaeger, J., Cook, N.G., Zimmerman, R., 2007. Fundamentals of Rock Mechanics. Wiley-Blackwell. 488 p.
Marone, C., Cox, S.J.D., 1994. Scaling of rock friction constitutive parameters - the effects of surface-roughness and cumulative offset on friction of gabbro. Pure Appl. Geophys. 143 (1–3), 359–385.
Mei, C., Wu, W., 2021. Fracture asperity evolution during the transition from stick slip to stable sliding. Philos. Trans. R. Soc. A, Math. Phys. Eng. Sci. 379 (2196).
Mochizuki, K., Yamada, T., Shinohara, M., Yamanaka, Y., Kanazawa, T., 2008. Weak interplate coupling by seamounts and repeating M similar to 7 earthquakes. Science 321 (5893), 1194–1197.
Noda, H., Lapusta, N., 2013. Stable creeping fault segments can become destructive as a result of dynamic weakening. Nature 493 (7433), 518.
Ohnaka, M., 1973. Experimental studies of stick-slip and their application to the earthquake source mechanism. J. Phys. Earth 21, 285–303.
Okubo, P.G., Dieterich, J.H., 1984. Effects of physical fault properties on frictional instabilities produced on simulated faults. J. Geophys. Res. 89 (NB7), 5817–5827.

Patton, F.D., 1966. Multiple modes of shear failure in rock. In: Proceedings Proc. 1st Congr. Int. Soc. Rock Mech., vol. 1. Lisbon. ISRM, pp. 509–513.
Persson, B.N.J., Albohr, O., Tartaglino, U., Volokitin, A.I., Tosatti, E., 2005. On the nature of surface roughness with application to contact mechanics, sealing, rubber friction and adhesion. J. Phys. Condens. Matter 17 (1), R1–R62.
Power, W.L., Tullis, T.E., Brown, S.R., Boitnott, G.N., Scholz, C.H., 1987. Roughness of natural fault surfaces. Geophys. Res. Lett. 14 (1), 29–32.
Power, W.L., Tullis, T.E., Weeks, J.D., 1988. Roughness and wear during brittle faulting. J. Geophys. Res., Solid Earth Planets 93 (B12), 15268–15278.
Rabinowicz, E., 1958. The intrinsic variables affecting the stick slip process. Proc. Phys. Soc. 71 (4), 665–675.
Rice, J.R., Ruina, A.L., 1983. Stability of steady frictional slipping. J. Appl. Mech. 50 (2), 343–349.
Rubinstein, S.M., Cohen, G., Fineberg, J., 2004. Detachment fronts and the onset of dynamic friction. Nature 430 (7003), 1005–1009.
Ruina, A., 1983. Slip instability and state variable friction laws. J. Geophys. Res. 88 (NB12), 359–370.
Sagy, A., Brodsky, E.E., 2009. Geometric and rheological asperities in an exposed fault zone. J. Geophys. Res., Solid Earth 114.
Sagy, A., Lyakhovsky, V., 2019. Stress patterns and failure around rough interlocked fault surface. J. Geophys. Res., Solid Earth 124 (7), 7138–7154.
Scuderi, M.M., Marone, C., Tinti, E., Di Stefano, G., Collettini, C., 2016. Precursory changes in seismic velocity for the spectrum of earthquake failure modes. Nat. Geosci. 9 (9), 695.
Shitrit, O., Hatzor, Y.H., Feinstein, S., Palchik, V., Vinegar, H.J., 2019. Static and dynamic elastic moduli of organic-rich chalk. Geophys. Prospect. 67 (3), 624–650.
Siman-Tov, S., Aharonov, E., Sagy, A., Emmanuel, S., 2013. Nanograins form carbonate fault mirrors. Geology 41 (6), 703–706.
Tal, Y., Goebel, T., Avouac, J.P., 2020. Experimental and modeling study of the effect of fault roughness on dynamic frictional sliding. Earth Planet. Sci. Lett. 536, 116133.
Tal, Y., Hager, B.H., 2018. Dynamic mortar finite element method for modeling of shear rupture on frictional rough surfaces. Comput. Mech. 61 (6), 699–716.
Wang, K.L., Bilek, S.L., 2011. Do subducting seamounts generate or stop large earthquakes? Geology 39 (9), 819–822.
Yamada, M., Mori, J., Matsushi, Y., 2016. Possible stick-slip behavior before the Rausu landslide inferred from repeating seismic events. Geophys. Res. Lett. 43 (17), 9038–9044.
Yamashita, F., Fukuyama, E., Xu, S.Q., Mizoguchi, K., Kawakata, H., Takizawa, S., 2018. Rupture preparation process controlled by surface roughness on meter-scale laboratory fault. Tectonophysics 733, 193–208.